Sensitivity and Interpretation of Zonal Mean Climate From Two Atmospheric General Circulation Models with Different Dynamical Cores

He Zhang[1], Minghua Zhang[1,2*], and Qing-cun Zeng[1]

1. ICCES, Institute of Atmospheric Physics, Chinese Academy of Sciences, Beijing, China

2. Stony Brook University, New York

Submit to **Monthly Weather Review**

[*] *Corresponding author address*: Minghua Zhang, SoMAS, Stony Brook University, Stony Brook, NY, 11794-5000, USA.
E-mail: mzhang@notes.cc.sunysb.edu

Comment [H1]: 本页末是张老师是通讯作者，所以是不是星花标注错位置了？确认一下

Abstract

The dynamical core of the Institute of Atmospheric Physics of Chinese Academy of Sciences Atmospheric General Circulation Model (IAP AGCM4.0) and the Eulerian dynamical core of Community Atmosphere Model (CAM3.1) are used with the same CAM3.1 physical parameterizations to study the sensitivity of simulated climate. We report that the model with the IAP dynamical core simulated a colder troposphere than that from the CAM3.1 core, reducing the CAM3.1 warm bias in the troposphere from above 2 K to less than 1 K. However, when the two dynamical cores are used in the idealized Held-Suarez tests without moisture physics, the IAP AGCM core simulated a warmer troposphere than that in CAM3.1. The causes of the differences in the full models and in the dry models are then investigated.

We show that the IAP dynamical core simulated weaker eddies in both the full physics and the dry models than those in the CAM due to different numerical approximations. In the dry IAP model, the weaker eddies cause smaller heat loss from poleward dynamical transport and thus warmer troposphere in the tropics and middle latitudes. When moist physics is included, however, weaker eddies also lead to weaker transport of water vapor and reduction of high clouds in the IAP model, which then causes a colder troposphere. Our results show how interactive physical processes can change the effect of a dynamical core on climate simulations.

1. Introduction

Dynamical core of an atmospheric general circulation model often refers to the formulation of the hydrodynamic equations of the atmosphere and the numerical algorithms to solve it. The governing equations among different models may be different, depending on the purpose of the model applications, such as hydrostatic versus non-hydrostatic models. But even when the governing equations are the same, when formulated differently, the discretization methods typically make them different, even if the same types of numerically schemes are used. This is the case for the two dynamical cores to be evaluated in this paper: one with transformed velocity as the control variables of air motion (the IAP core), and the other with the vorticity and divergence as control variables (the CAM core).

Different numerical schemes to solve the atmospheric governing equations have been used in different modeling centers. Ideally, with sufficiently high resolution, the different numerical schemes should converge to each other. But this has not been achieved. Therefore, improvement of dynamical cores has been an ongoing process in the climate modeling community. Some of the considerations of a numerical scheme include its accuracy, consistency, stability, conservation, and computational efficiency. Due to limited resolutions, certain benefits of these measures may not be realized.

There is therefore the need of understanding and verifying dynamical cores to assure the quality of simulated climate (Williamson 2007). Several idealized cases have been designed to specifically test the numerical robustness of the dynamical cores (Held and Suarez, 1980; Boer and Denis 1997; Polvani et al. 2004; Jablonowski and Williamson 2006). These have been very

Comment [H2]: 参考文献中是 Suarez，请确认一下，连同文中其他出现这个姓的一起确认一下。

valuable to understand the sensitivity of numerical solutions to different schemes and resolutions. Most of these tests are formulated without moist physics. Because the numerical approximations are flow dependent, it is also important to understand the behavior of atmospheric dynamical cores in real settings of the atmosphere with moist physics.

The objective of this paper is to investigate the impact of the IAP AGCM4.0 dynamical core on simulated climate. We compared results from two models with the same physics package (the CAM3.1 physics package of Collins et al. (2004)), one using the IAP dynamical core (referred as IAP model), and the other using Eulerian dynamical core of the CAM3.1 (referred as CAM model). We report how the interactive physical parameterizations change the sensitivities of the dynamical cores. To our knowledge, no study has investigated the different sensitivities between the dry and moist models.

We wish to point out that the two dynamical cores used in this paper represent past and current generations of cores. Many advances have been made in recent years that have led improvements of numerical schemes, including the formulation of equations, flexibilities of grids, dicretization methods, and computational efficiency (e.g., Taylor et al. 2008; Ringer et al. 2008; Baba et al. 2010; Donner et al. 2011). It is the authors' hope that results from the present study will be useful to interpret the sensitivities of model results with these more sophisticated dynamical cores also.

This paper is organized as follows. Brief descriptions of the IAP AGCM4.0 dynamical core

and the experiments are given in section 2. Section 3 compares the simulations of temperature and general circulation between IAP AGCM4.0 and CAM3.1. Results from the dry model and aqua planet tests are also represented, along with interpretation of the sensitivities. The last section contains a summary.

1. Model description and experimental setup

a. IAP Dynamical Core

The IAP AGCM4.0 has evolved from several earlier versions that have been documented in the literature (Zeng et al. 1989; Bi 1993; Liang 1996; Zuo 2003; Zhang 2009). It has been used to simulate atmospheric circulations and climate, including summer precipitation anomalies and spring dust storms in China (e.g., Zeng et al. 1997; Lin and Zeng 1997; Xue et al. 2001; Chen et al. 2004).

For the purpose of the present study, only the dynamical core is described. The model uses a finite-difference scheme with a terrain-following σ coordinate (Phillips 1957). A latitude-longitude grid with Arakawa's C grid staggering is used for the horizontal discretization (Arakawa and Lamb 1977). The horizontal grid structure was initially adapted from the Oregon State University two-layer model (Ghan et al. 1982), which could be further traced to the model at the University of California at Los Angeles, but the formulation of the controlling equations and the difference schemes are different in the IAP model, which contain several novel features and are described here.

First, the model equations are based on the baroclinic primitive equations with subtraction of standard stratification. The standard stratification is characterized by state variables $\tilde{T}(p), \tilde{\phi}(p)$ and $\tilde{p}_s(\theta,\lambda)$, which satisfy the following equations:

$$\begin{cases} R\tilde{T}(p) = -p\dfrac{\mathrm{d}\tilde{\phi}(p)}{\mathrm{d}p} \\ \tilde{p}\,|_{z=\tilde{z}_s(\theta,\lambda)} \equiv \tilde{p}_s(\theta,\lambda) \end{cases} \tag{1}$$

where T is the temperature, $\phi = gz$ is the geopotential, z the height, g the gravity acceleration, p the pressure, p_s the surface pressure, θ the co-latitude, λ the longitude, $\tilde{z}_s$ the elevation of earth's surface, and the superscript '~' denotes the "standard atmosphere". With the "standard atmosphere" removed, the controlling equations solve the perturbation fields denoted by prime:

$$\begin{cases} T'(\theta,\lambda,p,t) = T(\theta,\lambda,p,t) - \tilde{T}(p) \\ \phi'(\theta,\lambda,p,t) = \phi(\theta,\lambda,p,t) - \tilde{\phi}(p) \\ p'_{sa}(\theta,\lambda,t) = p_s(\theta,\lambda,t) - \tilde{p}_s(\theta,\lambda) \end{cases} \tag{2}$$

The purpose of subtracting the standard stratification in the dynamical core is to reduce truncation errors, especially over regions of high terrain such as the Tibet Plateau.

Second, the IAP model aims to conserve available energy rather than total energy. To facilitate the numerical design, it therefore used the following variable substitution, referred to as the IAP transform:

$$\begin{cases} (U,V,\Phi) \equiv (Pu, Pv, PRT'/b) \\ P \equiv \sqrt{p_{es}/p_0}, \quad p_{es} = p_s - p_t \end{cases} \tag{3}$$

where p_t=2.2 hPa is the pressure at the model top layer, p_0=1000 hPa, and b=87.8 m s^{-1} is the approximate value of $\tilde{C}_0^2$, which is the characteristic velocity of gravity-wave propagation of the standard atmosphere determined by $\tilde{C}_0{}^2 = R\left(\kappa\tilde{T} - \mathrm{d}\tilde{T}/\mathrm{d}\ln p\right)$, where $\kappa = R/c_p$, R the gas constant for dry air, and c_p the specific heat of dry air at constant pressure. After the subtraction

of standard stratification, with the IAP transform and the vertical coordinate $\sigma \equiv (p - p_t)/p_{es}$, the dynamical core can be written as:

$$\begin{cases} \dfrac{\partial U}{\partial t} = -\sum_{m=1}^{3} L_m(U) - P_\lambda - f^* V \\ \dfrac{\partial V}{\partial t} = -\sum_{m=1}^{3} L_m(V) - P_\theta + f^* U \\ \dfrac{\partial \Phi}{\partial t} = -\sum_{m=1}^{3} L_m(\Phi) + (1-\delta_p)\left[\tilde{C}_0^2/b + \delta \cdot \kappa \Phi / P\right]\left(\Omega^{(1)} + \Omega^{(2)}\right) \\ \dfrac{\partial}{\partial t}\left(\dfrac{p'_{sa}}{p_0}\right) + D(P) + \dfrac{\partial P^2 \dot{\sigma}}{\partial \sigma} = \dfrac{1}{p_0} \nabla \bullet \left(\tilde{\rho}_{sa} k_{sa} \nabla \dfrac{p'_{sa}}{\tilde{\rho}_{sa}}\right) \end{cases} \tag{4}$$

where $\delta_p \equiv p_t / p$, f^* is the Coriolis parameter determined by $f^* = 2\Omega\cos\theta + u\mathrm{ctg}\theta/a$ with a the earth radius, Ω the angular velocity of the earth rotation, $\tilde{\rho}_{sa} = \tilde{p}_s / R\tilde{T}_s$ is the density of the "standard atmosphere" at surface, k_{sa} is the dissipation coefficient, L_1 and L_2 are the horizontal advection operators and L_3 is the vertical convection operator, which are defined by

$$\begin{cases} L_1(F) \equiv \dfrac{1}{2a\sin\theta}\left(2\dfrac{\partial Fu}{\partial \lambda} - F\dfrac{\partial u}{\partial \lambda}\right) \\ L_2(F) \equiv \dfrac{1}{2a\sin\theta}\left(2\dfrac{\partial Fv\sin\theta}{\partial \theta} - F\dfrac{\partial v\sin\theta}{\partial \theta}\right) \\ L_3(F) \equiv \dfrac{1}{2}\left(2\dfrac{\partial F\dot{\sigma}}{\partial \sigma} - F\dfrac{\partial \dot{\sigma}}{\partial \sigma}\right) \end{cases} \tag{5}$$

The pressure gradient terms are calculated according to the following formulas:

$$\begin{cases} P_\lambda = P\dfrac{\partial \phi'}{a\sin\theta \partial \lambda} + \dfrac{b\Phi(1-\delta_p)}{p_{es}} \cdot \dfrac{\partial p_{es}}{a\sin\theta \partial \lambda} \\ P_\theta = P\dfrac{\partial \phi'}{a\partial \theta} + \dfrac{b\Phi(1-\delta_p)}{p_{es}} \cdot \dfrac{\partial p_{es}}{a\partial \theta} \end{cases} \tag{6}$$

and other terms are determined by

$$\begin{cases} \Omega^{(1)} \equiv \dfrac{P\dot{\sigma}}{\sigma} - \dfrac{1}{P}\left[D(P) + \dfrac{\partial P^2 \dot{\sigma}}{\partial \sigma} \right] \\ \Omega^{(2)} \equiv \dfrac{U}{p_{es}} \cdot \dfrac{\partial p_{es}}{a \sin\theta \partial \lambda} + \dfrac{V}{p_{es}} \cdot \dfrac{\partial p_{es}}{a \partial \theta} \\ D(P) \equiv \dfrac{1}{a \sin\theta} \left(\dfrac{\partial PU}{\partial \lambda} + \dfrac{\partial PV \sin\theta}{\partial \theta} \right) \end{cases} \tag{7}$$

δ in equations (4) is 0 with the standard stratification approximation. If it is set to 1, the set of equations becomes the same as the primitive equations that are commonly used.

The advantage of using the IAP transform is that the conservation of the sum of kinetic energy E_k, the available potential energy E_{ep}, and the available surface potential energy E_{es}, written as

$$\begin{cases} E_k = \dfrac{p_0}{2g} \int_0^1 \int_0^{2\pi} \int_0^{\pi} \left(U^2 + V^2 \right) a^2 \sin\theta \mathrm{d}\theta \mathrm{d}\lambda \mathrm{d}\sigma \\ E_{ep} = \dfrac{p_0}{2g} \int_0^1 \int_0^{2\pi} \int_0^{\pi} \Phi^2 a^2 \sin\theta \mathrm{d}\theta \mathrm{d}\lambda \mathrm{d}\sigma \\ E_{es} = \dfrac{1}{2g} \int_0^{2\pi} \int_0^{\pi} \dfrac{R\tilde{T}_s}{p_s} \left(p'_{sa} \right)^2 a^2 \sin\theta \mathrm{d}\theta \mathrm{d}\lambda \end{cases} \tag{8}$$

$\frac{\partial}{\partial t}\left(E_k + E_{ep} + E_{es} \right) = 0$ is satisfied its differential form under the standard stratification approximation of $\delta = 0$.

The central difference scheme is used to discretize the terms on the right hand sides of equations (4) with the Arakawa's C grid. Two calculations are applied in the model to alleviate the reduced gird-size problem in high latitudes. Poleward of 70^o, Fourier filtering is used to damp the high frequency waves. Between 30^o to 70^o, we discretize $\partial F / \partial \lambda$ by

$$\left(\frac{\partial F}{\partial \lambda} \right)_i = \alpha_j \cdot \frac{F_{i+\frac{1}{2}} - F_{i-\frac{1}{2}}}{\Delta \lambda} + \beta_j \cdot \frac{F_{i+\frac{3}{2}} - F_{i-\frac{3}{2}}}{\mathbf{3}\Delta \lambda} \ , \tag{9}$$

where the subscript *i* and *j* denote the *i*th and the *j*th grid points for longitudinal and latitudinal direction respectively. α_j and β_j are coefficients dependent on latitudes and satisfy $\alpha_j + \beta_j = \mathbf{1}$. β_j increases linearly from 0 at 30^o to 1 at 70^o (Zhang et al. 2009). Furthermore, we split the model equations (4) to integrate the advection terms (e.g. $\sum_{m=1}^{3} L_m(U)$) with time step 600s and the inertia-gravity wave terms (e.g. $P_\lambda + f^* V$) with time step 200s to economize CPU time.

The nonlinear iterative time integration method described in Zuo et al. (2004) is used in the model. For simplicity, the equation $\frac{\partial F}{\partial t} + A(F) = 0$ is considered here, where A is a nonlinear operator. The integration from time *n* to time *n*+1 follows

$$
\begin{aligned}
F_{(\mathbf{1})}^{n+\mathbf{1}} - F^n &= \Delta t \cdot A\left(F^n\right) \\
F_{(\mathbf{2})}^{n+\mathbf{1}} - F^n &= \Delta t \cdot A\left(F_{(\mathbf{1})}^{n+\mathbf{1}}\right) \\
F_{(\mathbf{3})}^{n+\mathbf{1}} - F^n &= \Delta t \cdot A\left(\frac{F_{(\mathbf{2})}^{n+\mathbf{1}} + F^n}{\mathbf{2}}\right) \\
&\vdots \\
F_{(\mathbf{2}m)}^{n+\mathbf{1}} - F^n &= \Delta t \cdot A\left(F_{(\mathbf{2}m-\mathbf{1})}^{n+\mathbf{1}}\right) \\
F_{(\mathbf{2}m+\mathbf{1})}^{n+\mathbf{1}} - F^n &= \Delta t \cdot A\left(\frac{F_{(\mathbf{2}m)}^{n+\mathbf{1}} + F^n}{\mathbf{2}}\right)
\end{aligned}
\tag{10}
$$

where *m*=1, 2, 3, … . For current version of IAP AGCM, the iterative time is 3 (*m*=1) which has better computational stability and effectively retrains short waves while preserves long waves.

The horizontal diffusion is a ∇^2 form similar to Washington and Kasahara (1970). The semi-Lagrangian method (Williamson and Rasch 1989) is used to solve the water vapor continuity equation. The same CAM3.1 physical package (see Collins et al. 2004 in details),

without any empirical physics parameters tuning, is adopted in this study. The time step for physics is 600s, and the physics package is coupled to the dynamics using the process-split method described in Williamson (2002). In our simulations, the vertical levels and their locations are set approximately the same as CAM3.1 (about 2.2 hPa at top of the model). The resolution uses 256 grids in longitudes and 128 grids in latitudes, which are the same as the grids in the T85 spectral resolution of CAM3.1. Based to simulation performance of the CAM3 with full physics, Williamson (2008) showed that the T85 spectral resolution is equivalent to about 1 degree resolution in the finite volume dynamical core. We therefore also carried out simulations using 1 degree resolutions as sensitivity experiments.

b. the CAM3.1dynamical core

The CAM3.1 has three different dynamical cores as well as different horizontal resolutions. The standard Eulerian spectral-transform mothod with horizontal resolution T85 is used in this paper. The time step for dynamical core and physical package are both 600s. Other details about the CAM3.1 are given in Collins et al. (2004). Main differences with the IAP dynamical include: (1) vorticity and divergence as dynamical control variations, (2) spectral representation of all linear terms and spectral-transform calculation of the quadratic terms, (3) bi-harmonic horizontal diffusion in the in most of the interior of the atmosphere versus harmonic diffusion in the IAP core, (4) conservation of available potential energy, and (5) subtraction of standard stratification in the IAP model.

c. experimental setup

The IAP AGCM4.0 and CAM3.1 are both integrated for 17 years respectively with the same physics package, and the boundary and initial data are interpolated from the same original data. Averages of simulations in the last 15 years are presented. The SST and sea ice datasets are climatological monthly datasets from blended products that combined the global Hadley Centre Sea Ice and Sea Surface Temperature (HadISST) dataset (Rayner et al. 2003) for years up to 1981 and the Smith/Reynolds EOF dataset (Reynolds et al. 2002) post-1981. The concentrations of greenhouse gases are held constant at their levels in 1990. The primary source of the validation data is NCEP/NCAR reanalysis (Kalnay et al. 1996). Both the model results and reanalysis data are truncated to T42 for direct comparison.

3. Results

a. Temperature and general circulation from climate simulations

We have examined a suite of atmospheric fields from the IAP AGCM4.0 by using the AMWG (Atmospheric Model Working Group) diagnostics package developed by NCAR (National Center for atmospheric Research) (http://www.cgd.ucar.edu/cms/mstevens/diagnostics). The overall performance is similar to the CAM3.1 that was described in Hurrell et al. (2006). In this paper, therefore, we only focus on the differences between the simulations of the IAP AGCM4.0 and the CAM3.1.

Figures 1a and 1b show the deviation of the zonally averaged temperature from the NCEP reanalysis in the models. The differences between the IAP AGCM4.0 and the CAM3.1 simulations are shown in Figure 1c. Shading indicates differences judged statistically significant

at the 0.05 level for a student test based on 15 yearly mean simulations. As in most of the AGCMs (Boer et al. 1992), there exists a notable cold bias near the polar tropopause in both models. Moreover, the CAM3.1 has a warm bias throughout most of the troposphere. This warm bias is systematically reduced in the model with the IAP dynamical core, especially in the tropical and subtropical regions between 30°N and 30°S, where the simulated temperature with the IAP core is colder than that in the CAM3.1 by 1-2 K, and this colder difference is statistically significant. Poleward of 50°N and 50°S, the IAP model simulated warmer troposphere than the CAM does. Since the two models used different polar filters, it is difficult to trace the causes of the differences at high latitudes. We therefore focus on the simulation differences in low and middle latitudes.

Distribution of zonal wind has traditionally been one of the fundamental measures of climate simulations. It is closely linked geostrophically to the temperature by thermal wind relation. Figures 2a to 2c show that both models simulated the main features of the observed zonal winds, including the westerly jet cores located near 200 hPa over the middle-latitudes of both hemispheres, and the tropical easterlies in the lower and middle troposphere as well as in the stratosphere. The two models all overestimated the intensity of the westerly jet in both hemispheres (Figures 2d and 2e). This overestimation however is reduced by about half in the IAP AGCM4.0 relative to the CAM3.1. The jets in the CAM3.1 are stronger than in the NCEP/NCAR reanalysis by 4-6 m s^{-1} and 6-8 m s^{-1} in Northern Hemisphere (NH) and SH respectively, while the corresponding biases with the IAP core are about 2 m s^{-1} and 4 m s^{-1}. This can be more clearly seen in the difference figure between the two models (Figure 2f).

Transports of heat and momentum by eddies are important mechanisms to establish the general circulation and maintain the energy balance as well as angular momentum conservation of the atmosphere. The observed climatological annual mean of zonally averaged transient eddy heat fluxes in Figure 3c shows two peaks of poleward heat fluxes in the lower and upper troposphere at middle latitudes. Both simulations with the IAP model (Figure 3a) and the CAM3.1 (Figure 3b) capture these two peaks pattern well. The NCEP reanalysis annual mean transient eddy heat flux $\overline{v'T'}$ is averaged from 12 monthly means calculated from daily data; the model $\overline{v'T'}$ is calculated by

$$\overline{v'T'} = \overline{vT} - \bar{v}\bar{T} \tag{11}$$

from instantaneous data, where the bar denotes the monthly mean and the prime denotes the deviation from the mean. This difference in the calculations may account for some of the differences between the model results and the NCEP reanalysis. But the emphasis of our study is on the difference of the two models. Figure 3d indicates the weaker poleward heat transport above 500 hPa in the IAP model.

The weaker eddies in the IAP model are more clearly seen in the eddy momentum transport of Figure 4. Since spectral models nominally represent a higher resolution than grid point models with the same number of grid points (Williamson 2008), there is the possibility that the more diffusive simulation in the IAP model is due to the "lower" resolution. We therefore conducted an additional simulation of the IAP AGCM4.0 with finer resolution 1^o x 1^o and compared the results against the CAM3.1 with T85 in Figure 5. It can be seen that the eddy

activities are also weaker in the finer resolution IAP AGCM4.0 compared to the CAM3.1.

b. Held-Suarez test

To contrast with the model with full physics, we next examine the impact of the dynamical core without moist physics by using the Held and Suarez (1994) experiment, hereafter referred to as H-S. The thermal forcing is Newtonian relaxation to a specified temperature field of varying time scale with latitudes and pressure. The momentum forcing is a sink represented by Rayleigh friction in the lower troposphere. The atmosphere is integrated without moist processes, topography, land-sea contrast and seasonal or diurnal cycle.

The initial data is not important in the H-S test, since after several months of integration, the prescribed forcing drives the model dynamics to quasi-equilibrium state that is independent of the initial state. In this paper, the integration of the model with the IAP dynamical core (referred to as IAP core) started from the same initial data as for the full model run. The CAM3.1 (referred to as CAM core) was integrated from an earlier run of a lower resolution T42 to avoid the computational instability caused by disequilibrium between wind and pressure gradient due to lack of topography. Both models were integrated for 1220 days. By discarding 200 days, the rest 1020 days are divided to 17 periods of 60 days. Independent 40 day samples are obtained by discarding 20 days in each period. The time -mean fields and statistics are taken from the 17 samples.

Figure 6 shows zonally averaged 17-periods mean temperature from the H-S tests with the

IAP core and CAM core and their difference with statistical test. The major feature of the real atmosphere is reproduced with the idealized forcing as what is expected. What is not expected however is that simulated troposphere in the IAP core is generally warmer than that in the CAM core, which is opposite to the results found in the climate simulations shown in Figure 1c. Associated with the warmer troposphere, the simulated westerly jets in the IAP core are stronger than those from the CAM core (Figure 7). This difference is also opposite to that in the climate simulations, in which the jets are weaker in the IAP model.

The distribution of simulated eddy heat flux from H-S tests is presented in Figure 8. The patterns of eddy heat fluxes of the H-S tests are similar to the climate simulations with two peaks located in lower and upper troposphere respectively. The difference between the two dynamical cores in Figure 8c is similar to the climate simulations in Figure 3d with weaker heat transport in the upper peak and equatorward shift of the lower peak. The eddy momentum fluxes simulated by two cores are shown in Figure 9. Consistent with the full models, the values of the maximum are smaller in the IAP core. Therefore, the IAP model simulated weaker eddy activities in both the model with full physics and in the dry model than those in CAM3.1, yet the IAP model simulated colder troposphere in the full physics model but warmer troposphere in the dry model than CAM3.1.

c. Aqua-planet test

Because the IAP core and the CAM3.1 core differ in their surface pressure calculation, we conducted aqua-planet experiments to examine the possible impact of the different treatment

of surface topography in the full models. The idealized control SST in Neale and Hoskins (2000) is used in this paper. The results from the aqua-planet tests by IAP AGCM4.0 (hereafter IAP aqua) and by CAM3.1 (hereafter CAM aqua) will be compared with the results from real climate simulations and from H-S tests.

As in Neale and Hoskins (2000), the aqua-planet simulations by the two models are integrated for 40 months, with the last 36 months used for the analysis. For simplicity, only the differences of the two models are given here (Figure 10). Relative to the CAM aqua, the following four features can be identified: (1) the IAP aqua simulated a colder troposphere (Figure 10a); (2) the westerly jet is weaker and displaced equatorward in the IAP aqua (Figure 10b); (3) the poleward eddy heat transport at middle latitude around 45°N and 45°S is weaker in the IAP aqua (Figure 10c); (4) the momentum transport is weaker in the IAP aqua (Figure 10d). The first two features are consistent with the differences between the two models with full physics, but opposite to those in the H-S tests. The last two features are consistent among all experiments.

These results confirm that the IAP dynamical core is more diffusive with less energetic eddies. It would be more satisfying if we can definitively attribute the weaker eddies in the IAP model to the specifics of a numerical scheme relative to the CAM3.1. Such attribution however is known to be very difficult. Previous studies have also shown large sensitivities of eddy kinetic energy to dynamical cores (Wan et al. 2008). The causes of these sensitivities can be due to possible factors such as the formulation of the controlling equations, the discretization method,

horizontal diffusions, and selection of different parameters. The second-order centered difference scheme in the IAP core is however likely an important factor. Held and Suarez (1994), after comparing a spectral core and fourth-order finite difference dynamical core, also noted that when a fourth-order version of the finite difference dynamical core was replaced by a second-order version, their model produced quite different simulations with much weaker eddies. With this sensitivity in mind, in the following, we focus on why weaker eddies in the IAP model caused colder troposphere in the model with full physics relative to CAM3.1, but warmer troposphere in the dry model.

d. Interaction between moist physics and dynamics

To aid the discussion, we write the zonally averaged temperature equation as

$$\frac{\partial \overline{\theta}}{\partial t} = -\frac{1}{a\cos\varphi}\frac{\partial \cos\varphi \overline{v\theta}}{\partial \varphi} - \frac{\partial \overline{\omega\theta}}{\partial p} + \overline{Q}, \tag{12}$$

in which, φ is the latitude; v is the meridional wind; ω the vertical velocity; θ the potential temperature; Q the diabatic heating; overbar denotes zonal average. Upon vertical integration from the surface (p_s) to the tropopause (p_t), the vertical transport term on the right hand side drops out, and using the quasi-geostrophic approximation (Andrews et al. 1987), we have

$$\int_{p_t}^{p_s} \overline{v\theta}dp = \int_{p_t}^{p_s} \overline{v}\,\overline{\theta}dp + \int_{p_t}^{p_s} \overline{v'\theta'}dp \approx \int_{p_t}^{p_s} \overline{v}_g\,\overline{\theta}dp + \int_{p_t}^{p_s} \overline{v'\theta'}dp = \int_{p_t}^{p_s} \overline{v'\theta'}dp \tag{13}$$

For the dry model, Q is specified as a relaxation to the radiative equilibrium temperature $\overline{\theta}_e$, which can be schematically written as

$$\overline{Q} = -\alpha\left(\overline{\theta} - \overline{\theta}_e\right) \tag{14}$$

where α is a relaxation coefficient. Substituting (13) and (14) into (12) and integrating over the

tropics from the equator to latitude φ_1 (say 30N), we get the following steady-state relationship between low-latitude temperature and eddy transport after some rearrangements:

$$\frac{1}{\cos\varphi_1}\iint_{\varphi=0,\varphi_1;p}(\alpha\bar{\theta})a\cos\varphi d\varphi dp=\frac{1}{\cos\varphi_1}\iint_{\varphi=0,\varphi_1;p}(\alpha\bar{\theta}_e)a\cos\varphi d\varphi dp-\int_p\overline{v'\theta'}|_{\varphi_1}\,dp \tag{15}$$

In the IAP dry model, the last term on the right hand side is smaller than that in the CAM3.1 because of weaker eddy activities. This explains why IAP-core simulated a warmer troposphere in low latitudes relative to CAM-core.

When moist physics is included, the diabatic heating is no longer in the simple form of equation (14). The weak eddies with the IAP dynamic core lead to weaker transport not only in heat, but also in moisture. Figures 11a and 11b show the three-dimensional transport tendencies of water vapor in the two models. Because water vapor decreases exponentially with height, only values in the middle and upper troposphere are shown. Upward and poleward transport of water vapor are seen in both models. Figure 11c shows the difference between the two models. It is seen that the transport is systematically weaker in the model with the IAP dynamical core.

This difference leads to a systematic difference in the relative humidity in the two models (Figure 12), which leads to difference in clouds as shown in Figure 13. The IAP dynamical core is drier than the CAM3.1, especially in the upper troposphere. The reduction of cloud amount in the upper troposphere reaches about twenty percent of the mean cloud amount. High clouds are greenhouse agents that trap infrared radiation to space. The smaller amount of high clouds in the IAP model corresponds to a cooling difference relative to the CAM model as in Figure 14 that shows the total radiative heating rate (qrl +qrs).

To demonstrate that it is indeed the cloud that caused the difference in the radiative heating, we carried out a series of offline radiation calculations. The set of calculations is listed in Table 1. For simplicity, we used the annual mean from climate simulation from the two moist models in the offline calculations. Figure 15a gives radiative heating difference between the offline calculations using the IAP and the CAM model output. The difference pattern is consistent with that in Figure 14c. There is a larger radiative cooling in most region of troposphere in IAP moist model compared to CAM moist model. Figure 15b shows the difference of heating rate due to change of clouds. It is seen that cloud fraction is the dominant contributor to the different radiative cooling between the two moist models, while temperature and water vapor have much smaller contributions (Fig. 15c, d). In addition to the radiative heating, the diabatic heating term in the thermodynamic equation of (12) is also contributed by latent heat and turbulent transport including convection. But these are found to be opposite to the difference in the total diabatic heating between the two models.

The impact of diabatic heating on the difference between the dry model and full model can be further illustrated in Figure 16, which gives a segment of the time evolution of the temperature tendency, and the contributions from dynamics and diabatic heating with the IAP core, in Figure 16a is for the dry H-S simulation, and in Figure 16b for the moist model. Here, the diabatic heating is calculated from physical parameterizations in the models, and the dynamical contribution is derived by total temperature tendency minus the diabatic heating. The frictional heating and the heating from energy fixer are classified to the diabatic heating, which

are small. It is seen that in the H-S test, the total temperature tendency closely follows the dynamical term. The variation of the contribution from the diabatic heating is smaller than that of the dynamical terms. Its maximum has a phase lag to the minimum in the total tendency. There is no significant correlation between adiabatic heating and dynamic tendency. However, in the moist model, there is significant negative correlation between adiabatic heating and the dynamic term. Namely, if there is a warming due to dynamic transport, there is an offsetting diabatic heating that quickly responds to cool the atmosphere. The variation of the diabatic heating is comparable to or can overcompensate that from the dynamical transport in driving the temperature variation.

4. Summary

The zonal mean temperature, wind and eddy fluxes with the IAP dynamical core and the Eulerian CAM3.1 dynamical core are evaluated. The results reveal that the tropical tropospheric temperature in the IAP model with full physics is colder than that in the CAM3.1 (and closer to NCEP reanalysis). But when the dynamical core is used in dry simulation, the IAP model simulated a warmer troposphere than the CAM3.1. Aqua-planet experiments are used to rule out the impact of different treatment of topography as the cause of the difference between the two models with full physics.

We have shown that the IAP dynamical core is more diffusive and with less energetic eddies relative to the CAM3.1. These are consistent among the experiments of dry and moist atmospheres. In the dry simulation, the less energetic eddies correspond to smaller heat transport

out of the low latitudes, which leads to a warmer tropical troposphere in the IAP model. In the moist simulation, however, the less energetic eddies also cause less upward transport of water vapor, and less high cloud amount in the IAP model. The reduced high clouds correspond to increased radiative cooling of the atmosphere in the IAP model, leading to a colder troposphere relative to CAM3.1.

Our study demonstrates how interactive moist physics, especially clouds, can change the behavior of a dynamical core in climate models. It points to the need to understand dynamical cores both in isolation and with full physics. To our knowledge, this is the first effort to report and analyze the cause of the opposite impact of dynamical core between dry and moist models on climate simulations.

Acknowledgments. We wish to thank the two anonymous reviewers of an earlier version of the paper, whose critical comments have led to significant improvement of the paper. We also wish to thank Dr. Wuyin Lin for his help and discussion in the course of this study. This research was supported by National Basic Research Program of China (973 Program) under Grant Nos. 2010CB951901 as well as the National Natural Science Foundation of China under Grant Nos. 41005054 and 40830103. Additional support is from the Climate Change and Prediction Program of the US Department of Energy, and the Modeling and Analysis Program of the National Administration for Space Studies to the Stony Brook University. Part of this research was carried out while the first author visited the Institute for Terrestrial and Planetary Atmosphere of the Stony brook University.

References

Andrews, D. G., J. R. Holton, and C. B. Leovy, 1987: Middle Atmosphere Dynamics, pp. 123-133.

Arakawa, A., and V. B. Lamb, 1977: Computational design of the basic dynamical process of the UCLA general circulation model. *Methods in Computational Physics*, **17**, Academic Press, 173-265.

Baba, Yuya, Keiko Takahashi, Takeshi Sugimura, Koji Goto, 2010: Dynamical Core of an Atmospheric General Circulation Model on a Yin–Yang Grid. *Mon. Wea. Rev.*, **138**, 3988–4005.

Bi, X., 1993: IAP 9L AGCM and climate simulation. Ph. D. dissertation (in Chinese), Institute of Atmospheric Physics, Chinese Academy of Sciences, 210 pp.

Boer, G. J., and Coauthors, 1992: Some results from an intercomparison of the climates simulated by 14 atmospheric general circulation models. *J. Geophys. Res.*, **97**, 12771–12786.

Boer, G. J., and B. Denis, 1997: Numerical convergence of the dynamics of a GCM. *Climate. Dyn.*, **13**, 359-374.

Chen, H., Z. Lin, and G. Zhou, 2004: Experimental dynamical prediction of spring dust storm events in China. *Climatic and Environmental Research* (in Chinese), **9**, 182-190.

Collins, W. D., and Coauthors, 2004: Description of the NCAR Community Atmosphere Model (CAM3.0). NCAR Technical Note NCAR/TN-464+STR, xii+214 pp.

Donner, Leo J., and Coauthors, 2011: The Dynamical Core, Physical Parameterizations, and Basic Simulation Characteristics of the Atmospheric Component AM3 of the GFDL

Comment [H3]: 文中未引用该文献

Global Coupled Model CM3. *J. Climate*, **24**, 3484–3519.

Ghan, S. 1982: A Documentation of the OSU two-level atmospheric general circulation model. Issue 35 of Report, Oregon State University Climate Research Institute, 395 pp.

Held, I. M., and M. J. Suarez, 1994: A proposal for the intercomparison of the dynamical cores of atmospheric general circulation models. *Bull. Amer. Meteor. Soc.*, **75**, 1825-1830.

Hurrell, J. W., J. J. Hack, A. S. Phillips, J. Caron, and J. Yin, 2006: The dynamical simulation of the Community Atmosphere Model version 3 (CAM3). *J. Climate*, **19**, 2162-2183.

Jablonowski, C., and D. L.Williamson, 2006: Baroclinic wave test case for Dynamical cores of GCMs. *Quart. J. Roy. Meteor. Soc.*, **132**, 2943-2976.

Kalnay, E., and Coauthors, 1996: The NCEP/NCAR 40-year reanalysis project. *Bull. Amer. Meteor. Soc.*, **77**, 437-471.

Liang, X., 1996: Description of a nine-level grid point atmospheric general circulation model. *Adv. Atmos. Sci.*, **13**, 269-298.

Lin, Z., and Q. Zeng, 1997: Simulation of East Asian summer monsoon by using an improved AGCM. *Adv. Atmos. Sci.*, **14**, 513-526.

Neale, R. B., and B. J. Hoskins, 2000: A standard test for AGCMs including their physical parameterizations: I: The proposal. *Atmos. Sci. Lett.*, **1**, 101-107.

Phillips, N. A., 1957: A coordinate system having some special advantages for numerical forecasting. *J. Meteor.*, **14**, 184–185.

Polvani, L. M., R. K. Scott, and S. J. Thomas, 2004: Numerically converged solutions of the global primitive equations for testing the dynamical core of atmospheric GCMs. *Mon. Wea. Rev.*, **132**, 2539-2552.

Rayner, N. A., and Coauthors, 2003: Global analyses of sea surface temperature, sea ice, and night marine air temperature since the late nineteenth century. *J. Geophys. Res.*, **108**, 4407, doi:10.1029/2002JD002670.

Reynolds, R. W., N. A. Rayner, T. M. Smith, D. C. Stokes, and W. Wang, 2002: An improved in situ and satellite SST analysis for climate. *J. Climate*, **15**, 1609-1625.

Ringler, T., L. Ju and M. Gunzburger, 2008, A multiresolution method for climate system modeling: application of spherical centroidal Voronoi tessellations. *Ocean Dynamics*, **58** (5-6), 475-498.

Taylor, M. A., J. Edwards, and A. St-Cyr, 2008: Petascale atmosphere models for the Community Climate System Model: New developments and evaluation of scalable dynamical cores. *J. Phys. Conf. Ser.*, **125**, 012023, doi:10.1088/1742-6596/125/1/012023.

Xue, F., X. Bi, and Y. Lin, 2001: Modelling the global monsoon system by IAP 9L AGCM. *Adv. Atmos. Sci.*, **18**, 404-412.

Wan, H., M. A. Giorgetta, and L. Bonaventura, 2008: Ensemble Held-Suarez test with a spectral transform model: variability, sensitivity, and convergence. *Mon. Wea. Rev*., **136**, 1075-1092.

Washington, W. M., and A. Kasahara, 1970: A January simulation experiment with the two-layer version of the NCAR global circulation model. *Mon. Wea. Rev*., **98**, 559-580.

Williamson, D. L., and P. J. Rasch, 1989: Two-dimensional semi-Lagrangian transport with shap-preserving interpolation. *Mon. Wea. Rev*., **117**: 102-129.

Williamson, D. L., 2002: Time-split versus process-split coupling of parameterizations and dynamical core. *Mon. Wea. Rev*., **130**: 2024-2041.

Williamson, D. L., 2007: The evolution of dynamical cores for global atmospheric models. *J. Meteor. Soc. Japan*, **85B,** 241–269.

Williamson, D. L., 2008: Equivalent finite volume and Eulerian spectral transform horizontal resolutions established from aqua-planet simulations. *Tellus*, **60A**, 839-847.

Zeng, Q., and Coauthors, 1989: Documentation of IAP Two-Level Atmospheric General Circulation Model. DOE/ER/60314-H1, TR044. 383 pp.

Zeng, Q., and Coauthors, 1997: Seasonal and extraseasonal predictions of summer monsoon precipitation by GCMs. *Adv. Atmos. Sci.*, **14**, 163-176.

Zhang, H., 2009: Development of IAP atmospheric general circulation model version 4.0 and its climate simulations. Ph. D. dissertation (in Chinese), Institute of Atmospheric Physics, Chinese Academy of Sciences, 194 pp.

Zhang, H., Z. Lin, and Q. Zeng, 2009: The computational scheme and the test for dynamical framework of IAP AGCM-4. *Chinese J. Atmos. Sci.* (in Chinese), **33**, 1267-1285.

Zuo, R., 2003: Development of new generation grid point atmospheric general circulation model with high resolution. Ph. D. dissertation (in Chinese), China People's Liberation Army University of Science and Technology, 328 pp.

Zuo, R., and Coauthors, 2004: Designing and climatic numerical modeling of 21-Level AGCM (IAP AGCM-III). Part I: Dynamical framework. *Chinese J. Atmos. Sci.* (in Chinese), **28**, 659-674.

Table 1. Design of offline radiation calculations, the fields with suffix 'CAM' are from climate simulation of CAM, while the fields with suffix 'IAP' are from climate simulation of IAP.

Experiment Name	**Sensitive Fields**		
	Temperature	**Specific Humidity**	**Cloud Fraction**
CAM_ctrl	T_CAM	Q_CAM	CLD_CAM
IAP_ctrl	T_IAP	Q_IAP	CLD_IAP
IAP_CLDonly	T_CAM	Q_CAM	CLD_IAP
IAP_Tonly	T_IAP	Q_CAM	CLD_CAM
IAP_Qonly	T_CAM	Q_IAP	CLD_CAM

Figure Captions

Fig.1. The biases of zonally averaged 15-year annual mean temperature from (a) IAP and (b) CAM simulations with contrast to NCEP reanalysis data, and (c) their difference (IAP - CAM). Contour intervals are 1 K between -3 K and 3 K but 2 K beyond in (a) and (b) and 0.5 K in (c). Shaded areas are judged to be significantly different by the student test at 0.05 significance levels.

Fig. 2. Zonally averaged 15-year annual mean zonal wind from (a) IAP , (b) CAM, (c) NCEP reanalysis data, the biases of (d) IAP and (e) CAM with contrast to NCEP reanalysis data, and (f) the difference of the two simulations (IAP - CAM). Contour intervals are 5 m s^{-1} in (a), (b) and (c), 2 m s^{-1} in (d) and (e), and 1 m s^{-1} in (f) . Shaded areas are judged to be significantly different by the student test at 0.05 significance levels.

Fig. 3. Zonally averaged 15-year annual mean transient eddy heat flux from (a) IAP, (b) CAM, (c) NCEP reanalysis data, and (d) the difference of the two simulations (IAP - CAM). Contour intervals are 3 K m s^{-1} in (a) and (b), 1 K m s^{-1} in (c) and (d). Shaded areas are judged to be significantly different by the student test at 0.05 significance levels.

Fig. 4. Same as Fig. 3, but for transient eddy momentum flux. Contour intervals are 10 m^2 s^{-2} in (a) and (b), and 4 m^2 s^{-2} in (c) and (d).

Fig. 5. Differences of zonally averaged 5-year annual mean transient eddy heat flux (a) and momentum flux (b) from the climate simulations between the IAP AGCM4.0 with resolution 1^o x 1^o and the CAM3.1 with resolution T85 (IAP -CAM). Contour intervals are 1 K m s^{-1} in (a) and 4 m^2 s^{-2} in (b).

Fig. 6. Zonally averaged 17-periods mean temperature from the Held-Suarez tests with the (a) IAP and (b) CAM dynamical cores, and (c) their difference (IAP - CAM). Contour intervals are 5 K in (a) and (b), 0.5 K in (c) . Shaded areas are judged to be significantly different by the student test at 0.05 significance levels.

Fig. 7. Same as Fig. 5, but for zonal wind. Contour intervals are 5 m s^{-1} in (a) and (b), and 1 m s^{-1} in (c).

Fig. 8. Same as Fig. 5, but for transient eddy heat flux. Contour intervals are 3 K m s^{-1} in (a) and (b), and 1 K m s^{-1} in (c).

Fig. 9. Same as Fig. 5, but for transient eddy momentum flux. Contour intervals are 10 m^2 s^{-2} in (a) and (b), and 2 m^2 s^{-2} in (c).

Fig. 10. The difference of zonally averaged annual mean between IAP and CAM from aqua planet tests: (a) temperature; (b) zonal wind; (c) transient eddy heat flux; (d) transient eddy momentum flux. Contour intervals are 0.5 K in (a), 2 m s^{-1} in (b), 1 K m s^{-1} in (c), and 3 m^2 s^{-2} in (d).

Fig. 11. Zonally averaged annual mean dynamical transport of moisture from (a) IAP and (b) CAM simulations, and (c) their difference (IAP - CAM). Contour values are 5 x10^{-2} g kg^{-1} day^{-1} in (a) and (b), 1 x10^{-2} g kg^{-1} day^{-1} in (c).

Fig. 12. Same as Fig. 11, but for relative humidity. Contour values are 10 percent in (a) and (b), 2 percent in (c).

Fig. 13. Cloud fraction used in experiment (a) IAP_CLDonly and (b) CAM_ctrl, and (c) their difference (IAP_CLDonly - CAM_ctrl). Contour values are 0.05 in (a) and (b), 0.02 in (c).

Fig. 14. Zonally averaged annual mean radiative diabatic heating (qrs and qrl for shortwave and longwave radiative heating respectively) rate from (a) IAP and (b) CAM simulations, and (c) their difference (IAP - CAM). Contour intervals are 0.4 K day^{-1} in (a) and (b), 0.1 K day^{-1} in (c).

Fig. 15. Differences of radiative diabatic heating rate from the sensitive experiments: (a) IAP_ctrl – CAM_ctrl, (b) IAP_CLDonly – CAM_ctrl, (c) IAP_Tonly – CAM_ctrl, (d) IAP_Qonly – CAM_ctrl. Contour intervals are 0.2 K day^{-1} in (a) an (b), 0.05 K day^{-1} in (c) and (d).

Fig. 16. Evolution of heating rate from the IAP model in (a) Held-Suarez test and (b) climate simulation in troposphere (150 hPa – 1000 hPa) at low latitude (30°S - 30°N). Solid square: diabatic heating rate, solid triangle: adiabatic heating rate, hollow circle: total heating rate. Unit:

10^{-6} K s^{-1}

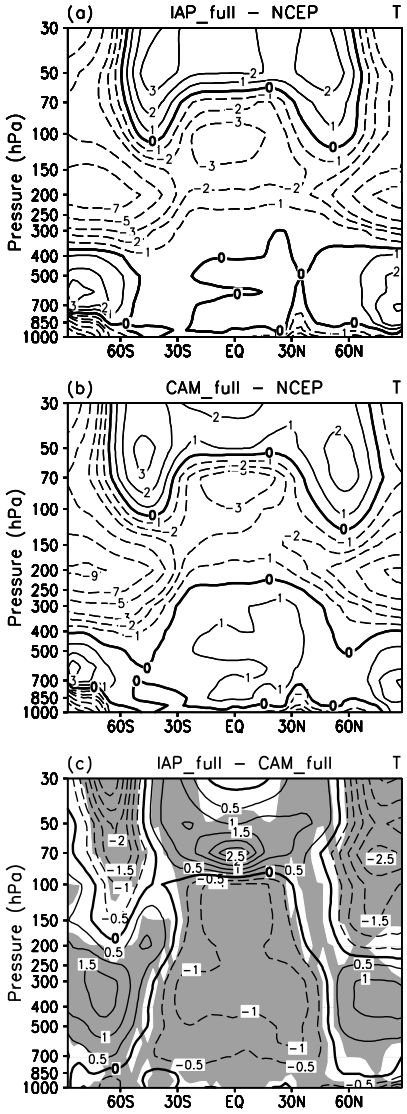

Fig.1. The biases of zonally averaged 15-year annual mean temperature from (a) IAP and (b) CAM simulations with contrast to NCEP reanalysis data, and (c) their difference (IAP - CAM). Contour intervals are 1 K between -3 K and 3 K but 2 K beyond in (a) and (b) and 0.5 K in (c).

Shaded areas are judged to be significantly different by the student test at 0.05 significance levels.

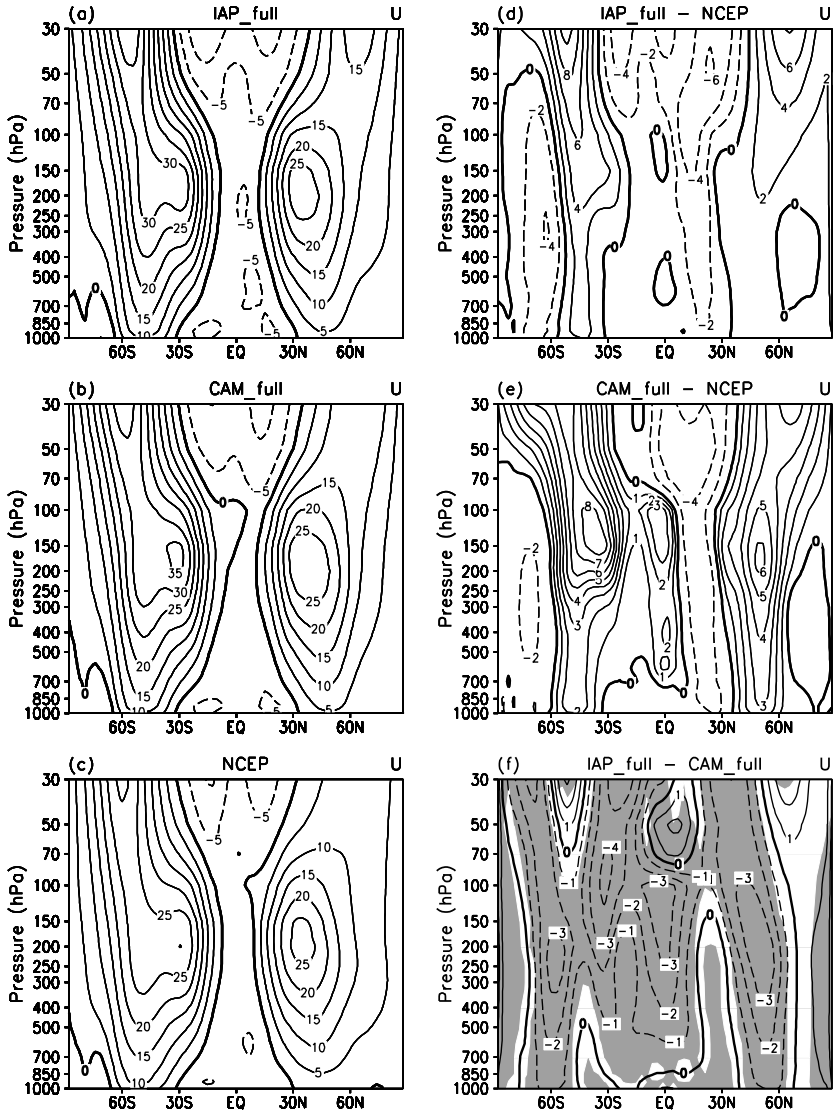

Fig. 2. Zonally averaged 15-year annual mean zonal wind from (a) IAP , (b) CAM, (c) NCEP reanalysis data, the biases of (d) IAP and (e) CAM with contrast to NCEP reanalysis data, and (f) the difference of the two simulations (IAP - CAM). Contour intervals are 5 m s^{-1} in (a), (b) and

(c), 2 m s^{-1} in (d) and (e), and 1 m s^{-1} in (f). Shaded areas are judged to be significantly different by the student test at 0.05 significance levels.

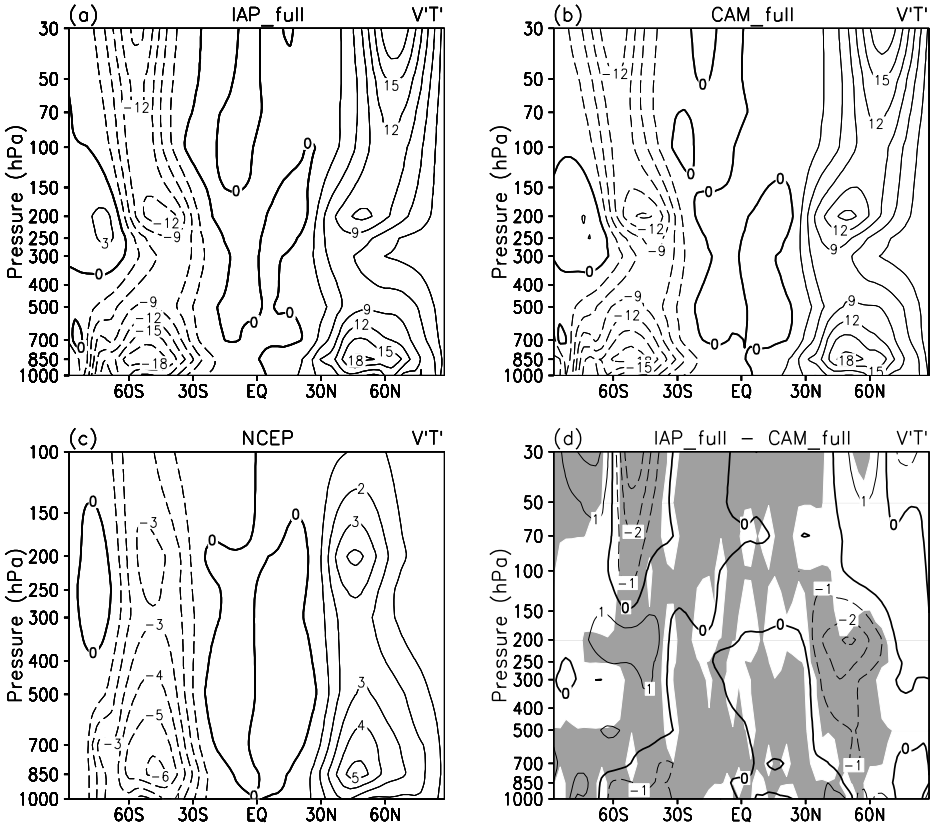

Fig. 3. Zonally averaged 15-year annual mean transient eddy heat flux from (a) IAP, (b) CAM, (c) NCEP reanalysis data, and (d) the difference of the two simulations (IAP - CAM). Contour intervals are 3 K m s^{-1} in (a) and (b), 1 K m s^{-1} in (c) and (d). Shaded areas are judged to be significantly different by the student test at 0.05 significance levels.

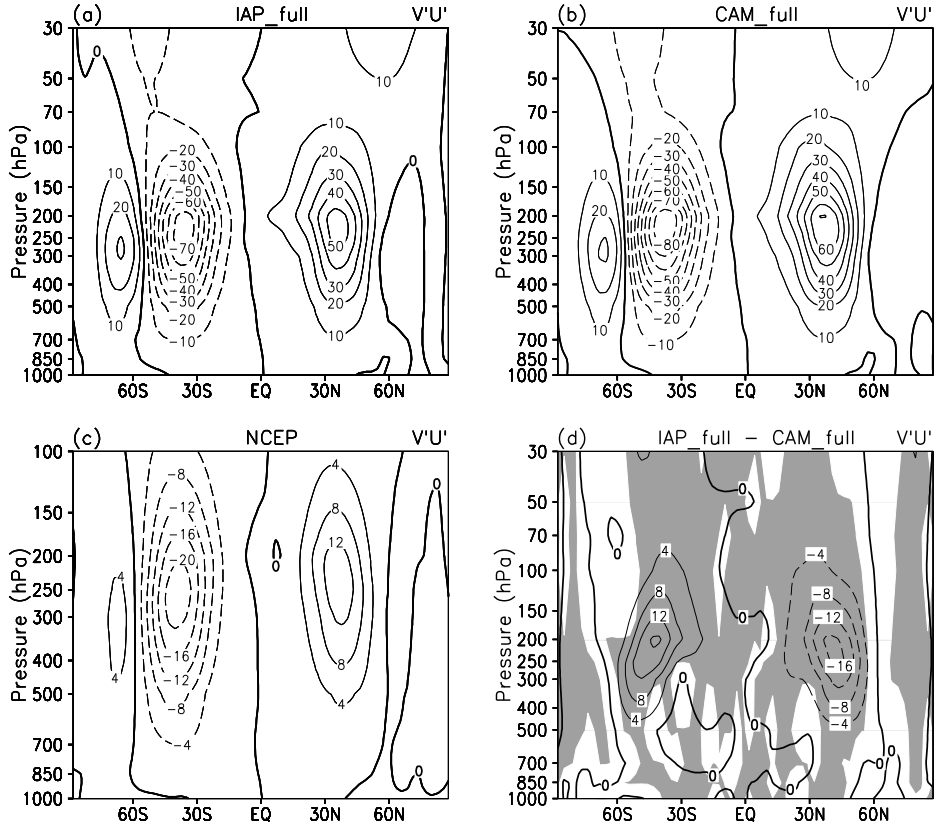

Fig. 4. Same as Fig. 3, but for transient eddy momentum flux. Contour intervals are 10 m^2 s^{-2} in (a) and (b), and 4 m^2 s^{-2} in (c) and (d).

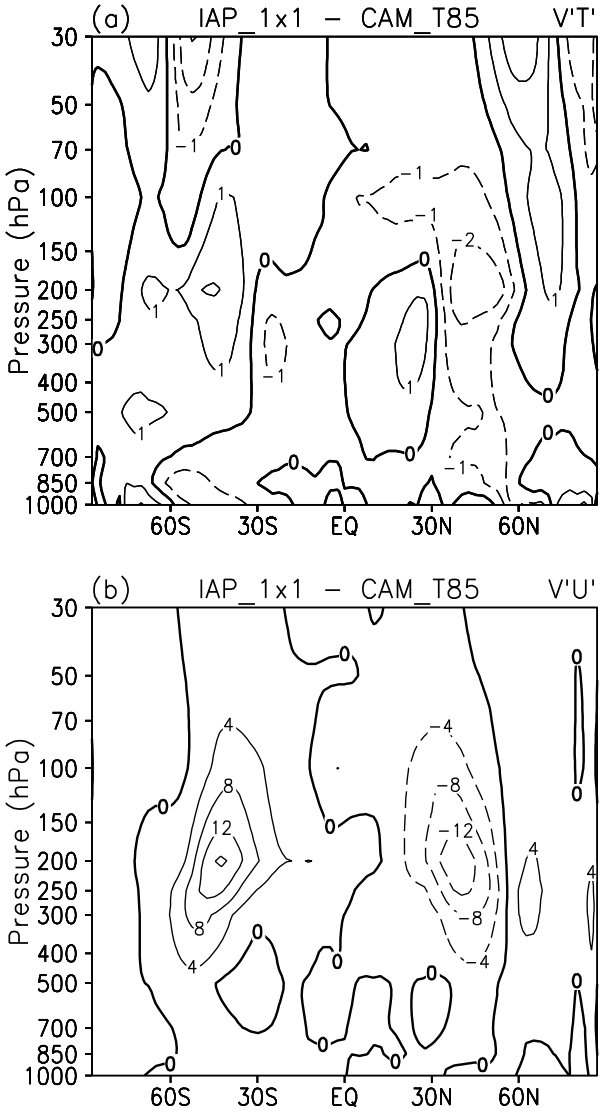

Fig. 5. Differences of zonally averaged 5-year annual mean transient eddy heat flux (a) and momentum flux (b) from the climate simulations between the IAP AGCM4.0 with resolution 1^{o} x 1^{o} and the CAM3.1 with resolution T85 (IAP -CAM). Contour intervals are 1 K m s^{-1} in (a) and 4 m^{2} s^{-2} in (b).

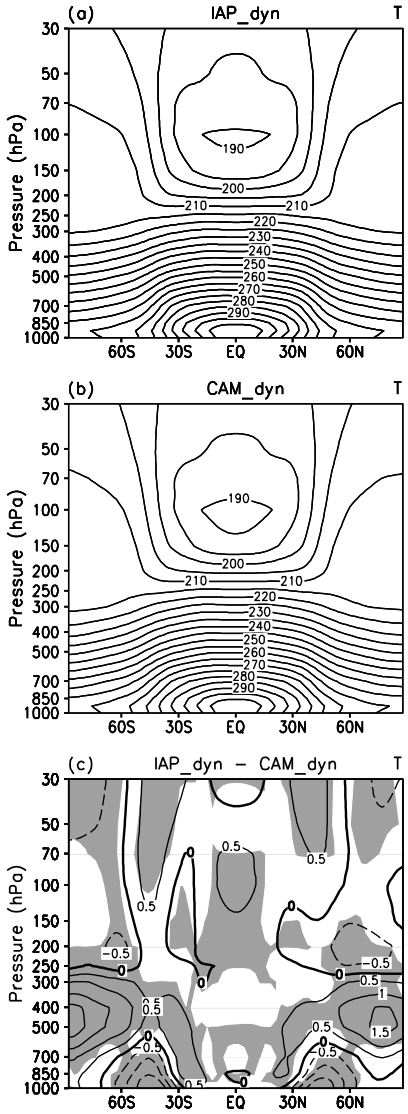

Fig. 6. Zonally averaged 17-periods mean temperature from the Held-Suarez tests with the (a) IAP and (b) CAM dynamical cores, and (c) their difference (IAP - CAM). Contour intervals are 5 K in (a) and (b), 0.5 K in (c). Shaded areas are judged to be significantly different by the student test at 0.05 significance levels.

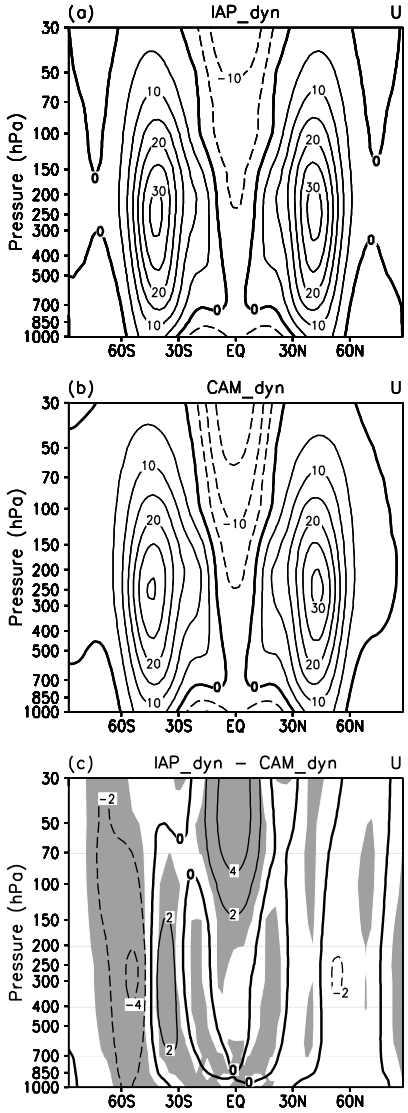

Fig. 7. Same as Fig. 5, but for zonal wind. Contour intervals are 5 m s^{-1} in (a) and (b), and 2 m s^{-1} in (c).

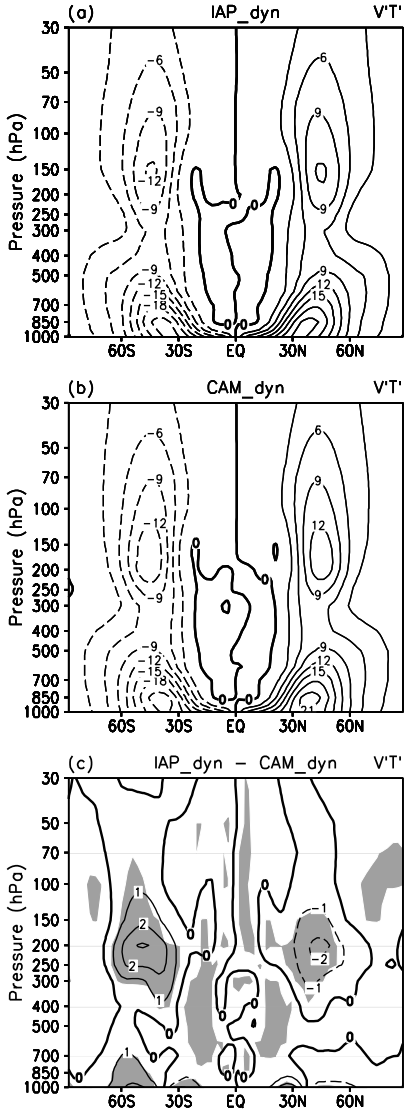

Fig. 8. Same as Fig. 5, but for transient eddy heat flux. Contour intervals are 3 K m s^{-1} in (a) and (b), and 1 K m s^{-1} in (c).

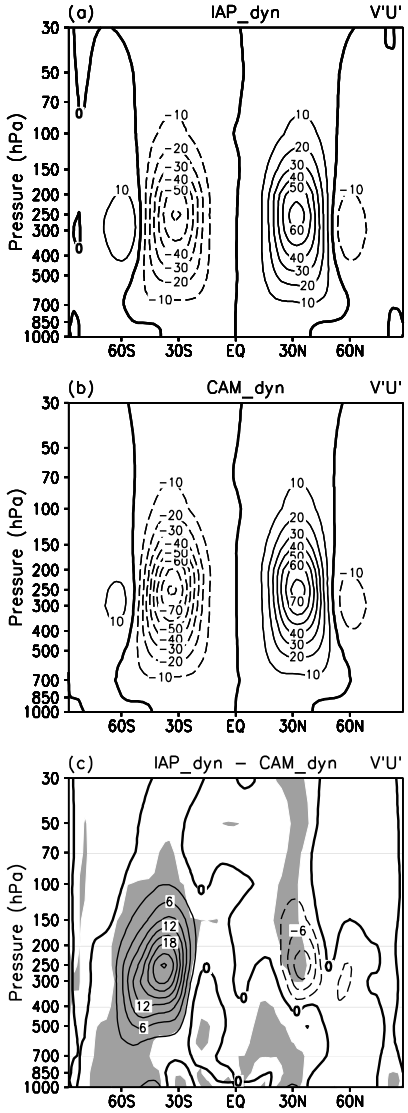

Fig. 9. Same as Fig. 5, but for transient eddy momentum flux. Contour intervals are 10 $m^2 s^{-2}$ in (a) and (b), and 3 $m^2 s^{-2}$ in (c).

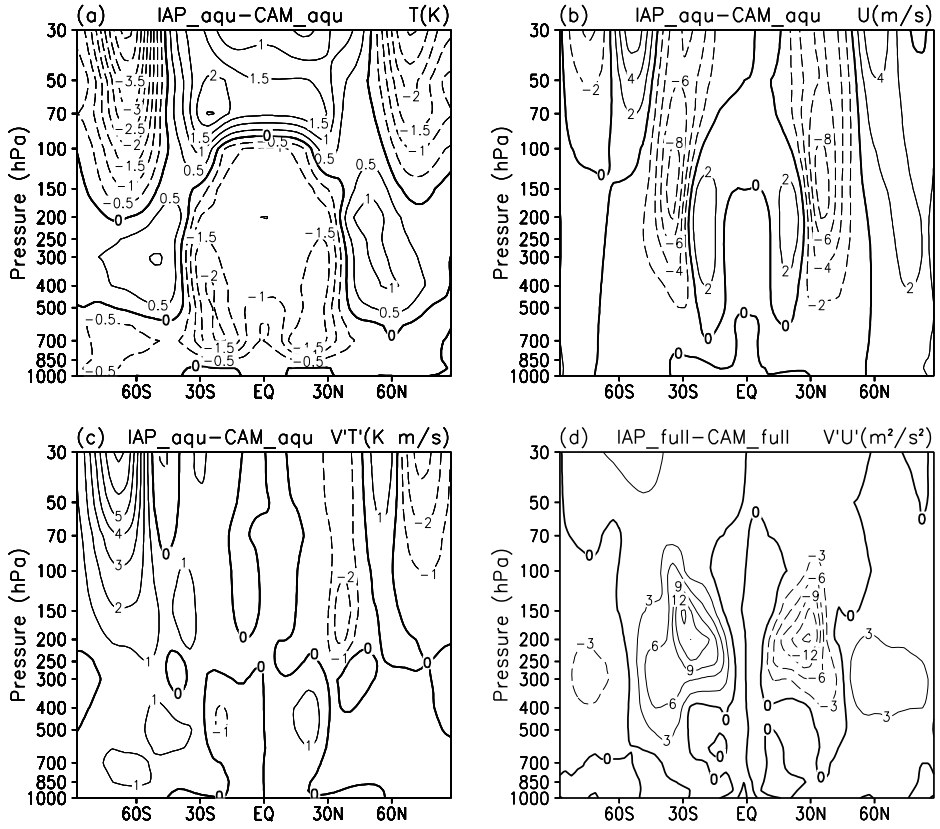

Fig. 10. The difference of zonally averaged annual mean between IAP and CAM from aqua planet tests: (a) temperature; (b) zonal wind; (c) transient eddy heat flux; (d) transient eddy momentum flux. Contour intervals are 0.5 K in (a), 2 m s^{-1} in (b), 1 K m s^{-1} in (c), and 3 m^2 s^{-2} in (d).

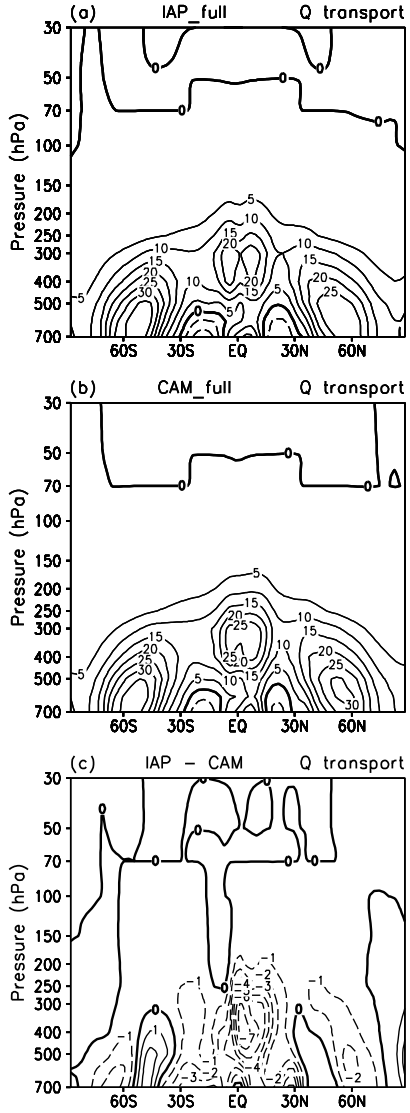

Fig. 11. Zonally averaged annual mean dynamical transport of moisture from (a) IAP and (b) CAM simulations, and (c) their difference (IAP - CAM). Contour values are 5 x10^{-2} g kg^{-1} day^{-1} in (a) and (b), 1 x10^{-2} g kg^{-1} day^{-1} in (c).

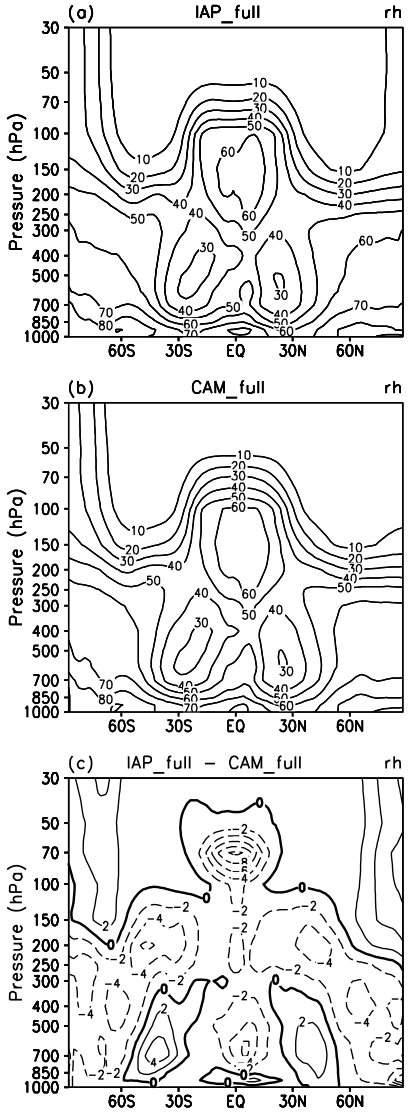

Fig. 12. Same as Fig. 11, but for relative humidity. Contour values are 10 percent in (a) and (b), 2 percent in (c).

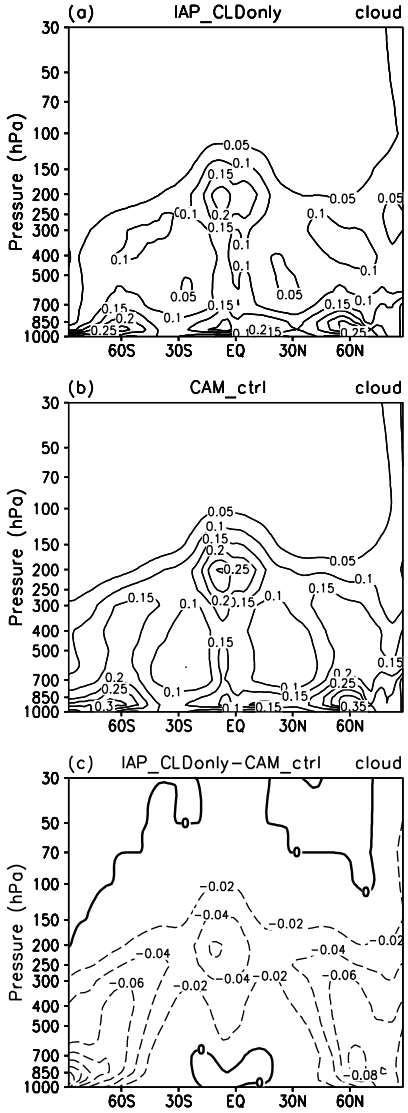

Fig. 13. Cloud fraction used in experiment (a) IAP_CLDonly and (b) CAM_ctrl, and (c) their difference (IAP_CLDonly - CAM_ctrl). Contour values are 0.05 in (a) and (b), 0.02 in (c).

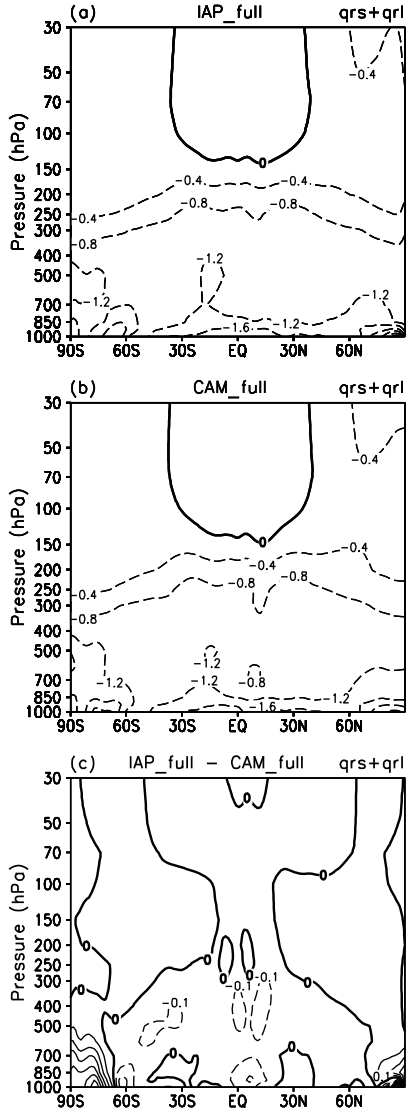

Fig. 14. Zonally averaged annual mean radiative diabatic heating rate (qrs and qrl for shortwave and longwave radiative heating respectively) from (a) IAP and (b) CAM simulations, and (c) their difference (IAP - CAM). Contour intervals are 0.4 K day^{-1} in (a) and (b), 0.1 K day^{-1} in (c).

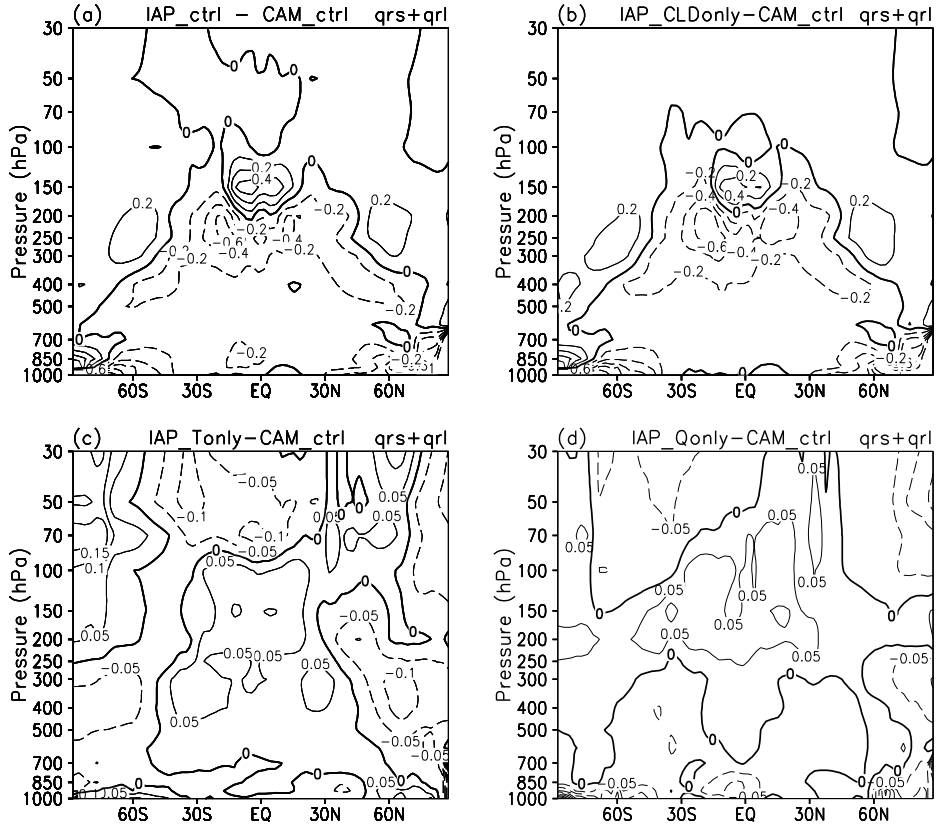

Fig. 15. Differences of radiative diabatic heating rate from the sensitive experiments: (a) IAP_ctrl − CAM_ctrl, (b) IAP_CLDonly − CAM_ctrl, (c) IAP_Tonly − CAM_ctrl, (d) IAP_Qonly − CAM_ctrl. Contour intervals are 0.2 K day^{-1} in (a) an (b), 0.05 K day^{-1} in (c) and (d).

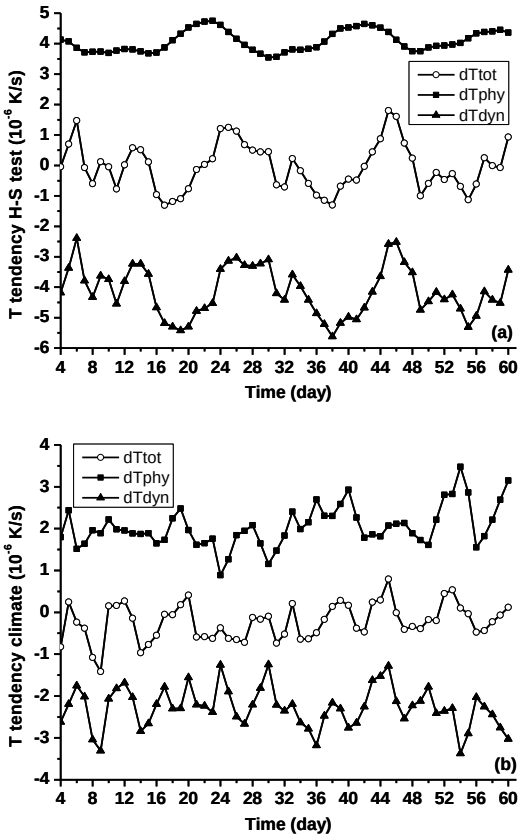

Fig. 16. Evolution of heating rate from the IAP model in (a) Held-Suarez test and (b) climate simulation in troposphere (150 hPa – 1000 hPa) at low latitude (30°S - 30°N). Solid square: diabatic heating rate, solid triangle: adiabatic heating rate, hollow circle: total heating rate. Unit: 10^{-6} K s^{-1}